Received: 7 March 2024 | Revised: 24 May 2024 | Accepted: 27 May 2024

DOI: 10.1002/jbio.202400090

JOURNAL OF BIOPHOTONICS

RESEARCH ARTICLE

Extraction of collagen morphological features from second-harmonic generation microscopy images via GLCM and CT analyses: A cross-laboratory study

R. Cicchi[1,2] | **E. Baria**[2,3] | **M. Mari**[4] | **G. Filippidis**[4] | **D. Chorvat**[5]

[1]National Institute of Optics, National Research Council, Florence, Italy

[2]European Laboratory for Non-Linear Spectroscopy (LENS), Sesto Fiorentino, Italy

[3]Department of Physics and Astronomy, University of Florence, Sesto Fiorentino, Italy

[4]Institute of Electronic Structure and Laser (IESL), Foundation for Research and Technology-Hellas (FORTH), Crete, Greece

[5]Department of Biophotonics, International Laser Centre (ILC), Slovak Centre of Scientific and Technical Information (SCSTI), Bratislava, Slovakia

Correspondence
E. Baria, Department of Physics and Astronomy, University of Florence, 50019 Sesto Fiorentino, Italy.
Email: baria@lens.unifi.it

Funding information
LASERLAB-EUROPE V, Grant/Award Number: 871124

Abstract

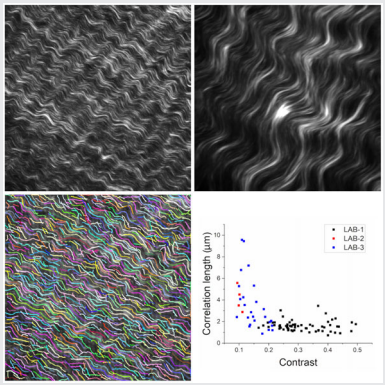

Second-harmonic generation (SHG) microscopy provides a high-resolution label-free approach for noninvasively detecting collagen organization and its pathological alterations. Up to date, several imaging analysis algorithms for extracting collagen morphological features from SHG images—such as fiber size and length, order and anisotropy—have been developed. However, the dependence of extracted features on experimental setting represents a significant obstacle for translating the methodology in the clinical practice. We tackled this problem by acquiring SHG images of the same kind of collagenous sample in various laboratories using different experimental setups and imaging conditions. The acquired images were analyzed by commonly used algorithms, such as gray-level co-occurrence matrix or curvelet transform; the extracted morphological features were compared, finding that they strongly depend on some experimental parameters, whereas they are almost independent from others. We conclude with useful suggestions for comparing results obtained in different labs using different experimental setups and conditions.

KEYWORDS
collagen, cross-laboratory, curvelet transform, equine pericardium, GLCM, morphology, SHG

1 | INTRODUCTION

The physiology and functionality of biological tissues are significantly conditioned by their microenvironment, which is in turn dependent on its components. In particular, the

Abbreviations: CT, curvelet transform; ECM, extracellular matrix; EP, equine pericardium; FOV, field of view; GLCM, gray-level co-occurrence matrix; SHG, second-harmonic generation.

extracellular matrix (ECM) is the major microenvironmental component and it plays a pivotal role in every physiological tissue function, including cellular motility [1], wound healing [2], tissue morphogenesis and perfusion [3], cancer proliferation and metastasis [4, 5], and aging [6]. The most abundant protein in the mammalian ECM is type I collagen, a molecule with a fibrillar hierarchical structure that strengthens and supports the structural units of biological tissues. The morphological organization of collagen type I within tissues significantly affects the architectural and biomechanical features of tissues, which are in turn connected to tissue physiology and functionality. Hence, the assessment of collagen organization is crucial for providing an exhaustive characterization of a biological tissue and for predicting its development. The submolecular arrangement of collagen, based on the hierarchical assembly of triple alpha-helix in a fibrillar structure, gives to the molecule a strong second-order nonlinear optical response [7], making it an ideal target for nonlinear imaging. Being a coherent technique, second-harmonic generation (SHG) microscopy is the ideal nonlinear optical modality for imaging collagen and for assessing its organization at multiple scales, from the molecular size to the supramolecular architectural level.

In the last years, SHG microscopy has been demonstrated extremely powerful to image collagen rich tissues [8], such as cornea [9, 10], tendon [11, 12], arteries [13, 14], human dermis [15–18], and animal scaffolds [19, 20]. SHG microscopy is able to highlight morphologic changes in collagen structure, which indicate particular diseases, such as keloid [21–23] and fibrosis [24–26], or altered physiologic conditions of various kinds of tissues, including muscle [27, 28], bones [29, 30], cartilages [31, 32], and thermally-treated samples [33–37]. In addition, SHG microscopy can probe collagen remodeling, a dynamic process that rearranges ECM in response to external stimuli and that is playing a key-role in the tumor development, since it significantly contributes to the formation and reshaping of tumor microenvironment. Several recent studies used collagen remodeling as a biomarker for breast [38–41], gastric [42], ovarian [43], colorectal [44], skin [45], and pancreatic cancer [46]. Collagen remodeling is a very important tissue biomarker, as it can be used as both diagnostic and prognostic indicator, so that it may help not only the pathologist to make a more accurate diagnosis but also the clinician to select the most appropriate therapeutic approach.

Up to date, several imaging analysis algorithms for extracting collagen morphological features from SHG images have been developed, mainly based on polarization scanning [47], intensity variations [48], Fourier transform [49], and filtering [50]. Recently, algorithms aimed at automatically measuring collagen fiber length and size, such as CurveAlign [51] or CT-FIRE [52], have emerged and became popular. Despite from these advancements, the dependence of the extracted morphological features to the experimental conditions and setup used represent a significant obstacle to the widespread of the methodology within the clinical diagnostics field. In fact, most of the SHG microscopy setups are custom-made or adapted from commercial instrument, making difficult the comparison of data obtained in different labs, as the experimental conditions are far from being reproducible. In this scenario, standardizing the processes of both image acquisition and analysis would be highly suitable in order to obtain the same morphological parameters when a sample is imaged in different labs and SHG images analyzed using the same algorithm.

In this study, we imaged samples of equine pericardium (EP), a standardized collagen scaffold used in tissue engineering applications [53], in three different labs with three different SHG microscopy setups. Acquired data are stored in an image database, hosted by the International Laser Centre (Bratislava, Slovakia). Acquired data were analyzed using gray-level co-occurrence matrix (GLCM) and CT-FIRE algorithms in order to derive information about correlation length and fiber size. The results were then compared highlighting the experimental parameters that mainly affect the values of derived parameters and suggesting preprocessing methods useful for standardizing SHG image analysis and compare data obtained in different labs with different experimental conditions.

2 | MATERIALS AND METHODS

2.1 | Sample preparation

Decellularized EP tissues in antibiotic solution (Matrix Patch™, Auto Tissue Berlin GmbH, Berlin, Germany) were placed between microscope slide and coverslip and imaged through SHG microscopy (Figure 1).

2.2 | Experimental apparatuses

The experiment was reproduced in three laboratories, each one with a different microscope from the others: LAB-1 at the National Institute of Optics, National Research Council, Italy; LAB-2 at the Institute of Electronic Structure and Laser, Foundation for Research and Technology-Hellas Greece; LAB-3 at Department of Biophotonics, International Laser Centre of SCSTI, Slovakia. Table 1 summarizes the most important parameters of these experimental setups.

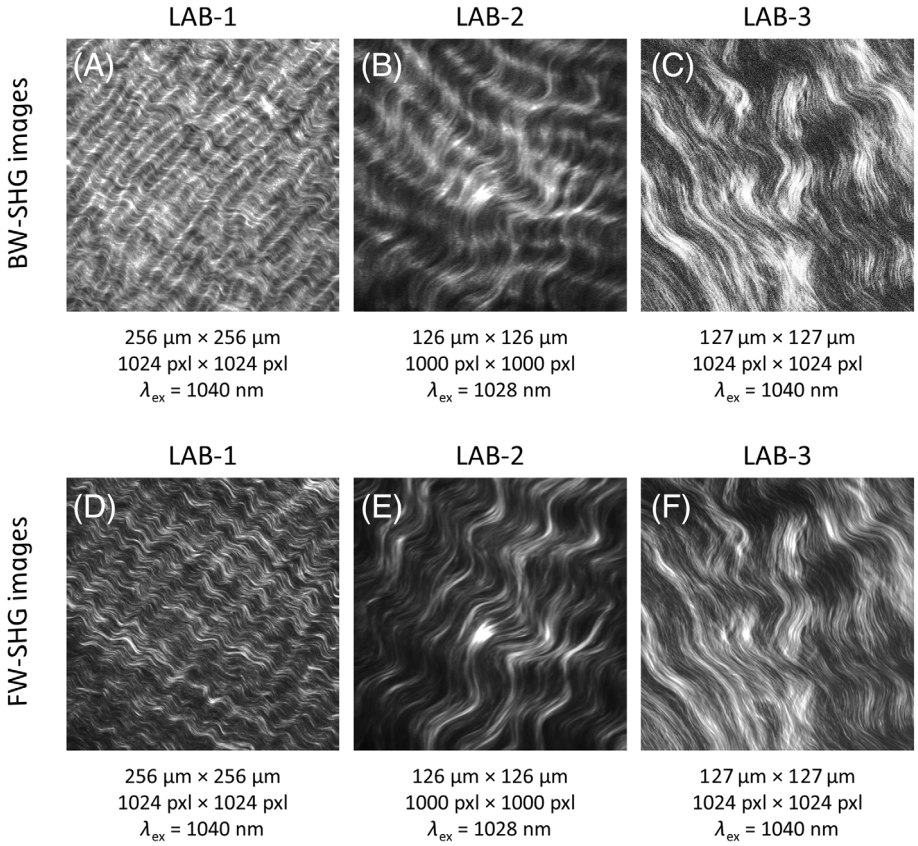

FIGURE 1 Examples of backward (BW)- (A–C) and forward (FW)-scattered (D–F) second-harmonic generation (SHG) images of equine pericardium samples, acquired in the three laboratories involved in this study using different experimental setups and settings, as detailed at the bottom of each image.

2.2.1 | LAB-1 microscope

This custom-made microscope has been described in greater detail in a previous publication [55]. It consists of four major parts: excitation source (Chameleon Discovery, Coherent, Santa Clara, CA, USA); laser power regulation and beam sizing; laser-scanning through galvanometric mirrors (Cambridge Technology, Bedford, MA, USA); backward and forward detection through two photomultiplier tubes (PMTs; H7422-40, Hamamatsu, Hamamatsu City, Japan). In particular, the excitation source is an Yb-based pulsed laser at 80 MHz rate with two synchronous outputs: the principal is tunable from 680 to 1300 nm with pulses of about 100 fs, while the auxiliary has a fixed wavelength at 1040 nm pulses of about 140 fs. Two quarter-wave plates ($\lambda/4$)—one for each beam—are used to achieve linear or circular polarization, and then both beams are superimposed on the same optical path. A removable, motorized half-wave plate ($\lambda/2$) can be used for rotating laser polarization on the sample plane. After passing through the scanning system, the laser beam is focused onto the sample by a Plan-Apochromat 20× dry objective lens (NA = 0.75, WD = 1 mm; Nikon, Nikon Minato, Tokyo, Japan); the same objective collects backward-emitted SHG signal, which is reflected by a longpass dichroic beamsplitter (FF665-Di02-25x36, Semrock Inc., New York, NY, USA) toward the first PMT. A 40× water-immersion objective (NA = 0.80, WD = 2 mm; Nikon, Nikon Minato, Tokyo, Japan) collects forward-emitted SHG signal, which is reflected by another longpass dichroic beamsplitter (FF665-Di02-25x36, Semrock Inc., New York, NY, USA) toward the second PMT. A narrow bandpass filter around the SHG wavelength (i.e., half of the excitation wavelength) is placed in front of each detector.

The experiment consisted in imaging 16 adjacent field of views (FOVs) of EP tissue—with each FOV being 256 µm × 256 µm in size and having 1024 pxl × 1024 pxl resolution—and was repeated for five excitation wavelengths on different tissue areas: 740, 800, 840, 900, and 1040 nm. Linear polarization was achieved for 800 and 840 nm and quasi-circular polarization for 740, 900, and 1040 nm. For linearly polarized light, a 180° polarization scan was performed with 18 steps (1 step every 10°), resulting in 18 SHG acquired images per FOV. For quasi-circularly polarized light, two mutually orthogonal polarizations were used. Finally, all images acquired on the same FOV were averaged together. For 800 nm excitation, only backward detection was performed; for all other wavelengths, both backward and forward signals were recorded.

TABLE 1 Imaging parameters of the three microscopes: laser wavelength, repetition rate and pulse duration, numerical aperture of the backward/forward objective, and corresponding theoretical resolution on the XY focal plane.

Setup	Excitation wavelength (nm)	Repetition rate (MHz)	Pulse duration (fs)	Numerical aperture BW/FW	Lateral resolution[a] BW/FW (nm)
LAB-1	740	80	100	0.75/0.80	442/417
LAB-1	800	80	100	0.75/0.80	478/N.A.
LAB-1	840	80	100	0.75/0.80	502/473
LAB-1	900	80	100	0.75/0.80	538/507
LAB-1	1040	80	100	0.75/0.80	621/586
LAB-2	1028	50	200	0.80/0.80	579/579
LAB-3	780	80	90	N.A./0.95	N.A./376
LAB-3	1040	50	170	1.2/0.95	405/501

Abbreviations: BW, backward; FW, forward.
[a]Derived from equations presented in Figure 4C in Reference [54].

2.2.2 | LAB-2 microscope

The second experimental setup is similar to the one described in previous studies [28, 41]. Briefly, an Yb-based femtosecond laser oscillator, emitting at a central wavelength of 1028 nm (Amplitude systems, 200 fs, 50 MHz) is employed as excitation source. The laser beam is guided to a modified upright microscope (Nikon). A set of galvanometric mirrors (Cambridge Technology) is utilized for the XY raster scanning of the sample. A zero-order half-wave retardation plate (WPH05ME; Thorlabs) is used in order to rotate the polarization of the incident beam. The focal plane is adjusted by using a motorized XYZ translation stage (Standa Ltd.). A moderate numerical aperture objective lens (Carl Zeiss, C-Achroplan 32×, NA = 0.8, water immersion) is used to tightly focus the beam onto the sample. The employed set up allows the simultaneous detection of nonlinear signals in forward and backward directions. The same objective used for the collection of backward-emitted SHG signals while a second objective lens (Carl Zeiss, PlanNeofluar, 40×, NA = 0.8, dry) is employed for the transmitted signals. Photomultiplier tubes (PMT Hamamatsu H9305-04) used for the recording of the signals. Proper bandpass interference filters (Semrock 514) are placed in front of the PMTs slots to solely detect the SHG signals arising from the EP samples.

The FOV of the system is 126 μm × 126 μm in size with 1000 pxl × 1000 pxl resolution. This defines a pixel size of 126 nm/pxl. To improve the signal to noise ratio (SNR), 10 scans were averaged for each final image. Images were recorded simultaneously both in reflection and in transmission modes. Two linear polarizations of the incident beam (mutually orthogonal) at the sample plane were employed. Various specimen regions were irradiated. 2D and 3D measurements were performed. For the 3D measurements, a series of 2D optical sections were obtained and projected (maximum intensity projection) onto a single plane.

2.2.3 | LAB-3 microscope

The third microscopy workstation was based on inverted microscope Axiovert 200M with confocal laser scanning head LSM 510 Meta NLO and motorized XY table (Carl Zeiss, Germany). For this study, the microscope was equipped with Zeiss C-Apochromat 40x/1.2 W Corr. objective with water immersion (NA = 1.2). SHG was induced by either Yb-based femtosecond oscillator with 1040 nm wavelength, 50 MHz repetition rate and 170 fs pulse duration (t-pulse 20, Amplitude Systemes, France) or femtosecond fiber laser with 780 nm wavelength, 80 MHz repetition rate and 90 fs pulse duration (Toptica FemtoFiber Smart 780, TOPTICA Photonics, Germany). The $\lambda/4$ waveplate was used to achieve circular polarization for both laser beams.

Spatial distribution of SHG signal from 1040 nm laser was detected in forward direction by transmission photodiode with short-pass NIR blocking filter (Thorlabs FESH750) and Zeiss interference wide-band filter green filter after collection by high-resolving condensor (NA = 1.4) used without immersion oil. For SHG detected in backward direction, we used internal confocal PMT detector using HFT KP 650 main beamsplitter and KP 685 short-pass emission filter for 1040 nm excitation wavelength. During the experiment, we averaged 16 adjacent scans of EP tissue with FOV being

127.1 μm × 127.1 μm (1040 nm excitation) or 130.3 μm × 130.3 μm (780 nm excitation) with 1024 pxl × 1024 pxl resolution and 12-bit depth, resulting in a pixel size of 124 and 127 nm/pxl in XY dimensions, respectively. For 3D measurements, we gathered series of planar optical sections within defined Z focus range of typically 24–36 μm with a 3–4 μm pitch.

2.3 | Image analysis

All SHG images recorded from EP were converted into .bmp files and analyzed through two different and well-known methods for studying tissue morphology: one based on GLCM and the other on curvelet transform (CT).

2.3.1 | GLCM features

GLCM is a method for examining the distribution of co-occurring, grayscale pixel values at a given offset [56], which is typically set to 1 (adjacent pixels). Functions based on GLCM are widely used for texture analysis [57] and, in particular, for extracting features such as Contrast, Correlation, Energy, and Homogeneity within an image. Contrast measures the local variations in the GLCM; Correlation measures the joint probability occurrence of the specified pixel pairs; Energy calculates the sum of squared elements in the GLCM; and Homogeneity measures the closeness of the distribution of elements in the GLCM to its diagonal. Another feature can be obtained from the Correlation Function of an image, that is, by calculating GLCM Correlation at different offsets [58]. The half-decay length of such function is known as the Correlation Length and can be used for evaluating the typical size of structures within the image.

Two custom-made Matlab (Mathworks, Natick, Massachusetts) routines were used to analyze SHG images and extract, respectively, the GLCM features (Contrast, Correlation, Energy, and Homogeneity) and the GLCM Correlation function. Finally, a custom-made program for LabVIEW (National Instruments, Austin, Texas) was used to extract the Correlation Length from the Correlation Function.

GLCM analysis was performed twice on all images. First, SHG images were analyzed with their original resolution: 250 nm/pxl (LAB-1), 126 nm/pxl (LAB-2), 124 and 127 nm/pxl (LAB-3). Then, all images were preprocessed in order to have approximately equal size and resolution, that is ∼125 μm × 125 μm and ∼ 250 nm/pxl, respectively: LAB-1 images were divided in 4; LAB-2 and LAB-3 images were rescaled in order to have half of the original number of pixels.

2.3.2 | CT-FIRE

CT-FIRE [59] is a freely available software developed by the Laboratory for Optical and Computational Instrumentation of the University of Wisconsin-Madison for automatically extracting fiber information from SHG images of collagen. In particular, we used CT-FIRE for evaluating the average width of all collagen fibers imaged by the three laboratories. Width values extracted by the software were converted from pxl to μm and averaged together for each excitation wavelength and microscope.

CT-FIRE analysis was also performed twice on all images: once with their original resolution, and then after being rescaled (as mentioned above).

3 | RESULTS AND DISCUSSION

3.1 | CT-FIRE algorithm

Among the recently developed image analysis algorithms useful for application to SHG images of collagen, CT-FIRE became increasingly popular during the last years. In order to better understand how the experimental conditions affect the morphological parameters of collagen fibers derived by CT-FIRE, we analyzed images of the same type of sample (EP), acquired in different labs using different excitation wavelengths, as well as different spatial features for scanning. Being a nonlinear scattering process, SHG should depend from excitation wavelength only in terms of intensity, as the SHG cross-section might vary with wavelength, while the morphological features of collagen—fiber thickness, length, straightness, and angular distribution—should be almost independent from the excitation wavelength used.

In this study, we focused our attention on fiber width estimation. When varying the scanning resolution, intended as the size of an individual pixel of the image, this extracted morphological parameter can vary dramatically, as shown in Figure 2A for forward-scattered and Figure 2C for backward-scattered SHG, where the values of "fiber width" extracted from images acquired in different labs using different scanning resolutions and excitation wavelengths are compared. Interestingly, these differences disappear when properly rescaling images in order to lead them back all to the same scanning resolution. In fact, Figure 2B,D shows the behaviors of the parameter "fiber width," extracted from CT-FIRE routine from the same image set as in Figure 2A,C, respectively, with the only difference that images have been rescaled in order to have the same scanning resolution in every image, as a function of the excitation wavelength. The "fiber width" resulted almost independent from the

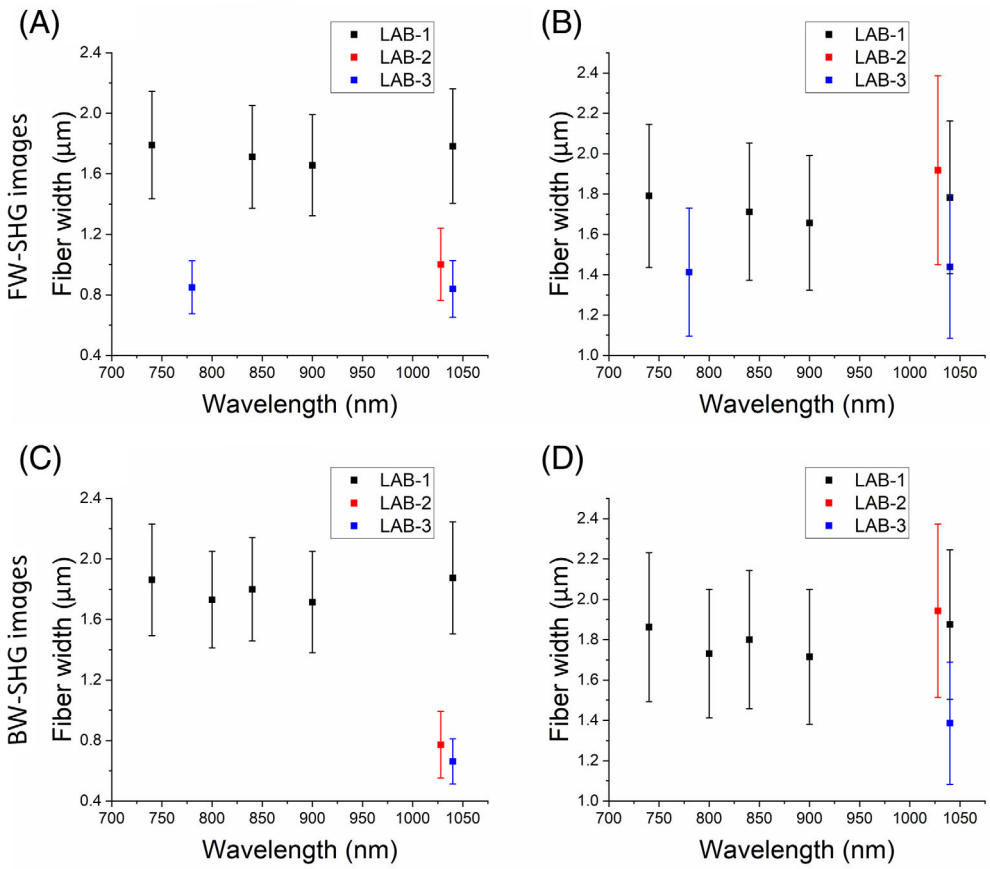

FIGURE 2 Left column: collagen fiber width ± standard deviation (SD) calculated using CT-FIRE routine from forward (FW)-scattered second-harmonic generation (SHG) images (A) and from backward (BW)-scattered SHG images (C), acquired using different excitation wavelengths in different labs with different experimental conditions. Right column: collagen fiber width ± SD calculated after image rescaling for correcting scanning resolution of FW-scattered (B) and BW-scattered SHG images (D).

excitation wavelength, demonstrating that this experimental condition does not influence the extracted morphological parameter, although the spatial resolution might vary proportionally. In summary, once the images are rescaled, we did not observe significant differences for the parameter "fiber width" when comparing images acquired in different labs, independently from the collection geometry used for detecting the SHG signal. This result demonstrates that particular attention has to be devoted to the scanning resolution when comparing SHG images of collagenous samples acquired using different experimental conditions and analyzed using the CT-FIRE routine.

3.2 | GLCM algorithm

The same set of images analyzed using CT-FIRE routine have been analyzed also with another popular image analysis method for SHG images based on GLCM. In fact, among the statistical parameters that can be extracted from GLCM analysis, Correlation is playing an important role, since it can provide information about periodical structures in the image, as well as sudden change or regularity of a fibrillar structure. For these reasons, GLCM Correlation has been used frequently for analyzing SHG images of fibrillar collagen. Despite the popularity of GLCM Correlation analysis, how the experimental conditions and imaging parameters affect the extracted values has not been explored so far.

As a first test, we compared GLCM features extracted from image acquired in two different labs when using the same excitation wavelength and detection geometry but different scanning resolution. As for CT-FIRE analysis shown in Figure 2, we demonstrated that the GLCM features, that have significantly different values when comparing data obtained from different labs without any correction, become comparable when data are rescaled in order to obtain the same scanning resolution. Figure 3 highlights this result by showing the values of GLCM features calculated form images before (Figure 3A) and after the correction (Figure 3B) for scanning resolution.

Then, forward-scattered (F-SHG) and backward-scattered SHG (B-SHG) images of the same specimen were compared. In particular, we calculated GLCM Correlation for both F-SHG and B-SHG images, finding significantly different results despite the images were coregistered. By looking at the two SHG images of the same FOV, F-SHG seems associated to higher contrast as compared with the corresponding B-SHG images (Figures 1 and 4). This is something that can be expected,

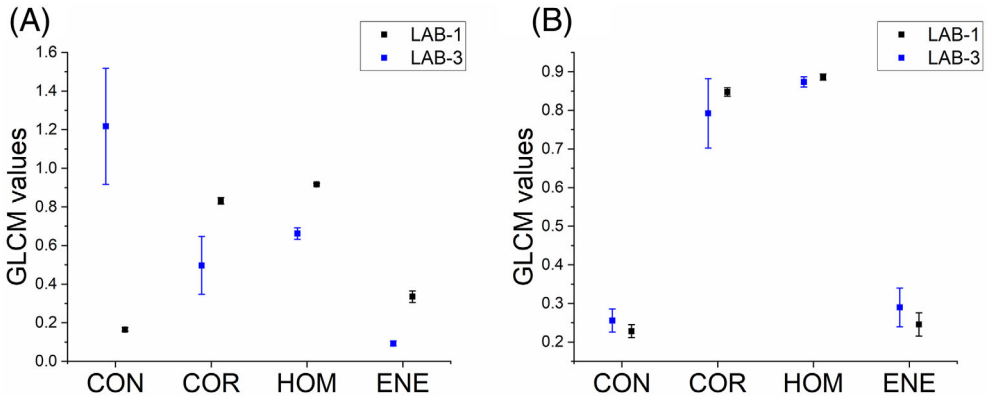

FIGURE 3 (A) Gray-level co-occurrence matrix (GLCM) features Contrast (CON), Correlation (COR), Homogeneity (HOM), and Energy (ENE) ± SDs, calculated from second-harmonic generation images acquired in two different laboratories using the same excitation wavelength (1040 nm) and detection geometry (backward) but different scanning resolution. (B) GLCM features ± SDs, calculated after having rescaled the images and corrected for scanning resolution for comparison.

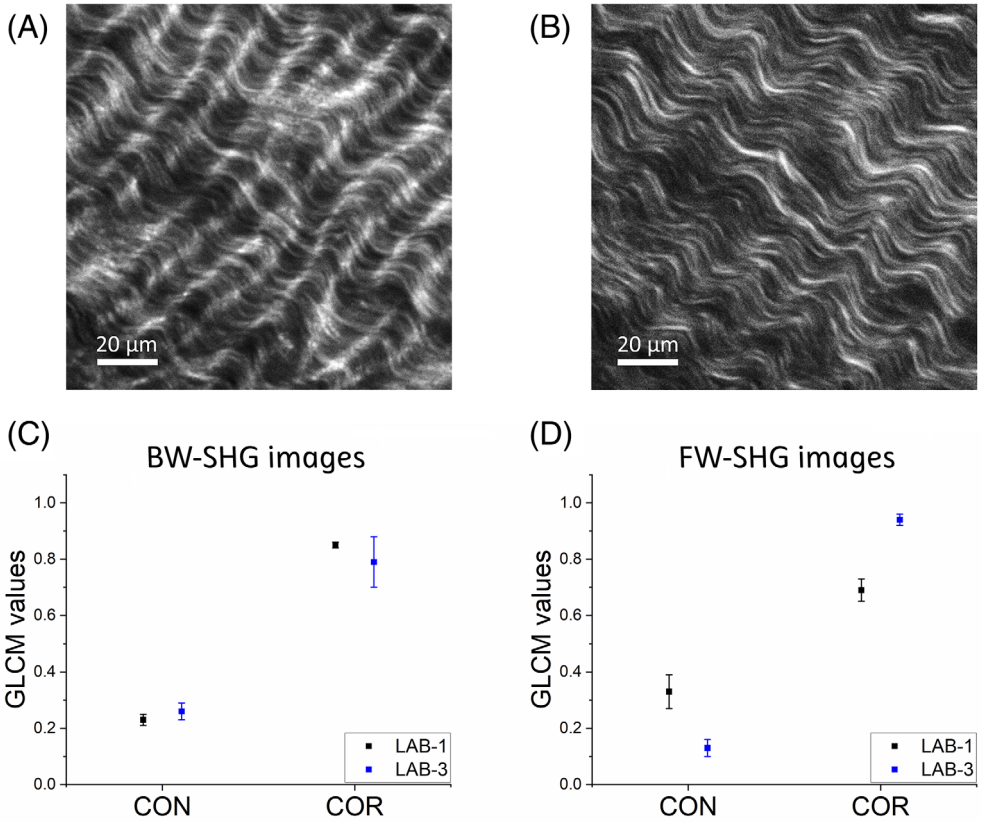

FIGURE 4 Backward (BW)- (A) and forward (FW)- (B) scattered second-harmonic generation (SHG) images acquired from the same field of view of a sample of equine pericardium using 1040 nm as excitation wavelength. Gray-level co-occurrence matrix (GLCM) features Contrast (CON) and Correlation (COR) ± SDs, calculated from BW-scattered SHG images (C) and from FW-scattered SHG images (D), acquired in LAB-1 (black squares) and LAB-3 (blue squares) using 1040 nm excitation.

since the forward-scattered SHG component is always more intense with respect to the backward-scattered component, while both images have zero-background, as this is a peculiar feature of SHG. When measuring image contrast through GLCM analysis, we found that a low GLCM Contrast value is associated to a high value of GLCM Correlation and vice versa, high GLCM contrast values correspond to low values of GLCM Correlation.

The dependence of these two parameters becomes more evident when examining results obtained from SHG images acquired in different labs using different excitation wavelengths and experimental parameters. More in detail, Figure 5 shows a graph where the values of GLCM Correlation length are plotted versus GLCM Contrast for a large dataset of SHG images of the same specimen acquired in different conditions. When imaging collagen fibers, the latter parameter may be used as an

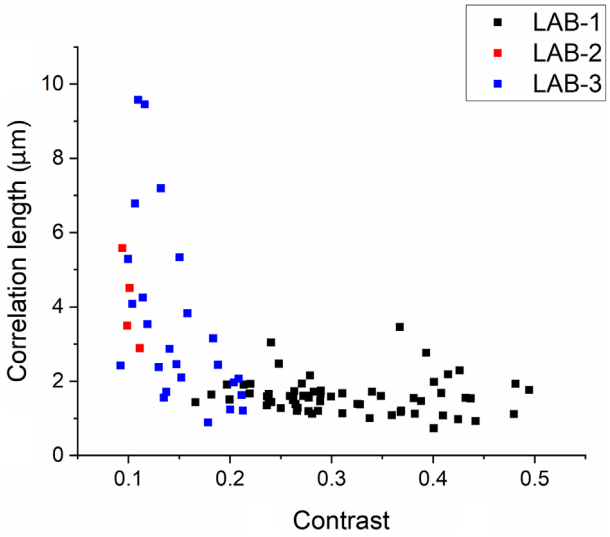

FIGURE 5 Gray-level co-occurrence matrix (GLCM) Correlation length plotted versus GLCM Contrast for forward-acquired second-harmonic generation images recorded in different laboratories, rescaled for correcting scanning resolution, and analyzed using GLCM-based analysis.

indicator for the SNR, while the former can be related to the average fiber width [21]. For small values of GLCM Contrast, we found that the Correlation length is inversely proportional to it, as already evidenced in the previous analysis on F-SHG and B-SHG images. The decrease of GLCM Correlation length with increasing GLCM Contrast continues up to a certain value of GLCM Contrast before reaching a saturation around ~1.6 μm. Once this value is reached, for higher values of GLCM Contrast, the two parameters appear independent, so that GLCM Correlation length is maintained on a constant value independently from the increase of GLCM Contrast. A possible interpretation is that image noise beyond a certain level may cause an artefactual increase in Correlation length, leading to an overestimation of average fiber size; on the contrary, once the SNR is sufficiently high, GLCM Correlation stabilizes around the value corresponding to fiber width.

This result demonstrates that the GLCM Correlation parameter, very often taken as feature parameter in the analysis of SHG images, has to be always considered in tandem with GLCM Contrast and, possibly, the analysis has to be limited to images exhibiting a GLCM Contrast beyond a specific value in order to extract GLCM Correlation parameters that are significant descriptors of the analyzed image.

3.3 | Discussion

Based on recent developments, the possibility to use SHG microscopy as a complementary microscopic tool within the histopathological lab is becoming more and more concrete. In fact, several studies have demonstrated the diagnostic performances of SHG microscopy on various type of tumors, which are indirectly diagnosed and characterized on the basis of the morphological response of collagen to the presence of malignancy, rather than analyzing malignant cells. Such approach offers a significant advantage over standard histopathological techniques, as it can be implemented without any tissue staining, and potentially without any tissue processing. Despite the promising performances, it is quite difficult to widespread SHG technology within a clinical scenario for multiple reasons. As first, histopathologists are trained on H&E images, whereas they are not use to the images acquired using SHG as contrast mechanism, making the interpretation and classification of images more difficult. This problem could be partially solved by means of solutions based on artificial intelligence, aimed at transferring the diagnostic performances achievable using SHG images to the H&E world, thanks to double-acquisition training and algorithms based on convolutional neural networks in order to realize a so-called "virtual staining" of the specimens [60]. Despite these advancements, other technical and economic limitations are preventing the adoption of SHG microscopy as a standard for tissue diagnostics at the histopathological level. In fact, SHG microscopes are in general completely custom instruments or custom implementations around commercial multiphoton fluorescence microscopes. In any case, commercial standardized solutions for SHG microscopy are currently not available on the market and custom solutions have a high cost with respect to traditional optical microscopy scheme. This prevents the widespread of the technology among histopathological labs, since a specialized skilled technician is required for developing, maintaining and using the microscope, and the cost of an instrument for SHG microscopy is not negligible.

The lack of a standard commercial instrument makes difficult comparing data obtained in different labs, as the experimental conditions are far from being reproducible. Although SHG should not depend heavily on the instrumentation performances, important experimental settings such as laser peak power or polarization state might significantly affect the detected signal and consequently the value of the extracted parameter. Anyway, the detected SHG signal should depend on the peak power only in terms of signal intensity. Furthermore, the potential effects resulting from the adoption of different polarization states can be mitigated by reproducing circularly polarized excitation via polarization scanning or an average of mutually orthogonal states. It would be difficult to standardize the polarization of different setups beyond this level, however, due to the custom

implementation of a typical SHG microscope: even when adopting identical optical elements, microscope internal arrangements—which in most cases are not disclosed by the manufacturer—could also affect the polarization state. Nonetheless, using imperfect polarization states (e.g., an elliptical polarization in place of a circular one) may slightly decrease SHG intensity along one axis of the image, without significantly affecting the extraction of collagen morphological features.

For these reasons, after standardizing the polarization state of the excitation in the three labs involved in this study, we employed analytical methods that are almost independent on the detected intensity to allow comparison of images acquired with different setups. Further, we standardized the size of the FOV and, in some cases, the number of acquired pixels per image. Nevertheless, the results obtained in different labs were different, unless the images were opportunely preprocessed, demonstrating that the obtained results strongly depend on a parameter that is apparently irrelevant to the employed analyses, the pixel size. Additionally, the dependence of the GLCM Correlation Length upon the parameter GLCM Contrast demonstrates that the signal to noise ratio is crucial for an efficient and precise extraction of morphological parameters from SHG images. Considering that the SNR depends not only by the laser peak power but also by the different collection efficiency of the experimental setups, which are in turn dependent on the objective lens used, on the detector sensitivity, on the detection optical scheme and geometry, those parameters are difficult to be standardized among different setups and they have to be carefully considered when comparing data acquired from different labs. These considerations are not limited to SHG but are valid in general, independently from the contrast mechanism used. In summary, this manuscript represents an initial attempt of tackling this problem by highlighting few limitations of commonly used image analysis algorithms for SHG images of collagen and providing some useful suggestions for both data acquisitions and comparison among different labs and instruments.

4 | CONCLUSION

In conclusion, this study highlighted the fact that morphological parameters extracted by the CT-FIRE routine are affected by the scanning resolution used, so that a particular attention has to be devoted to this acquisition parameter when CT-FIRE analysis of the acquired images is planned. In addition, by examining image analyzed using GLCM approach, we found that the GLCM Correlation parameter is strongly dependent on the GLCM Contrast of the examined image, so that the two parameters have to be evaluated in tandem when this kind of analysis is implemented. In this scenario, our experiment demonstrates that a lot of work has still to be done in order to standardize the processes of both image acquisition and analysis in SHG microscopy and to pave the way for wide spreading the technology in a clinical scenario. Nonetheless, SHG microscopy represents a powerful diagnostic tool assisting the pathologist and it could soon find a stable place in a clinical setting.

AUTHOR CONTRIBUTIONS

G. F. and R. C. were involved in conceptualization, investigation, writing (original draft, review, and editing), and data analysis. M. M. and E. B. were involved in data acquisition, data analysis, and writing (review and editing). D. C. was involved in project management, data acquisition, and writing (review and editing).

ACKNOWLEDGMENTS

The research leading to these results has received funding from LASERLAB-EUROPE (grant agreement no. 871124, European Union's Horizon 2020 research and innovation programme).

CONFLICT OF INTEREST STATEMENT

The authors declare no conflicts of interest.

DATA AVAILABILITY STATEMENT

The data that support the findings of this study are publicly available at https://microscopy.mlc.sk/omero/webclient/?show=project-323 ("SHG-Collagen-Cross-Lab-Study-2024"). OMERO database is based on the work of the team of J. R. Swedlow, University of Dundee, UK [61].

ORCID

E. Baria https://orcid.org/0000-0001-9679-7736
M. Mari https://orcid.org/0000-0002-5248-7485
G. Filippidis https://orcid.org/0000-0003-4748-5968

REFERENCES

[1] K. M. Yamada, J. W. Collins, D. A. Cruz Walma, A. D. Doyle, S. Gonzalez Morales, J. Lu, K. Matsumoto, S. S. Nazari, R. Sekiguchi, Y. Shinsato, S. Wang, *Int. J. Exp. Pathol.* **2019**, *100*, 144.
[2] M. Xue, C. J. Jackson, *Adv. Wound Care* **2015**, *4*, 119.
[3] G. E. Davis, D. R. Senger, *Circ. Res.* **2005**, *97*, 1093.
[4] C. Walker, E. Mojares, A. Del Río Hernández, *Int. J. Mol. Sci.* **2018**, *19*, 3028.
[5] J. Winkler, A. Abisoye-Ogunniyan, K. J. Metcalf, Z. Werb, *Nat. Commun.* **2020**, *11*, 5120.
[6] H. L. Birch, *Subcell. Biochem.* **2018**, *90*, 169.

[7] S. Roth, I. Freund, *J. Chem. Phys.* **1979**, *70*, 1637.
[8] G. Cox, E. Kable, A. Jones, I. Fraser, F. Manconi, M. D. Gorrell, *J. Struct. Biol.* **2003**, *141*, 53.
[9] M. Han, G. Giese, J. F. Bille, *Opt. Express* **2005**, *13*, 5791.
[10] A. T. Yeh, N. Nassif, A. Zoumi, B. J. Tromberg, *Opt. Lett.* **2002**, *27*, 2082.
[11] P. Stoller, B.-M. Kim, A. M. Rubenchik, K. M. Reiser, L. B. Da Silva, *J. Biomed. Opt.* **2002**, *7*, 205.
[12] T. A. Theodossiou, C. Thrasivoulou, C. Ekwobi, D. L. Becker, *Biophys. J.* **2006**, *91*, 4665.
[13] A. Zoumi, X. Lu, G. S. Kassab, B. J. Tromberg, *Biophys. J.* **2004**, *87*, 2778.
[14] R. Cicchi, C. Matthäus, T. Meyer, A. Lattermann, B. Dietzek, B. R. Brehm, J. Popp, F. S. Pavone, *J. Biophotonics* **2014**, *7*, 135.
[15] P. Stoller, K. M. Reiser, P. M. Celliers, A. M. Rubenchik, *Biophys. J.* **2002**, *82*, 3330.
[16] P. J. Su, W.-L. Chen, J.-B. Hong, T.-H. Li, R.-J. Wu, C.-K. Chou, S.-J. Chen, C. Hu, S.-J. Lin, C.-Y. Dong, *Opt. Express* **2009**, *17*, 11161.
[17] R. Cicchi, S. Sestini, V. De Giorgi, D. Massi, T. Lotti, F. S. Pavone, *J. Biophotonics* **2008**, *1*, 62.
[18] A. M. Pena, D. Fagot, C. Olive, J.-F. Michelet, J.-B. Galey, F. Leroy, E. Beaurepaire, J.-L. Martin, A. Colonna, M.-C. Schanne-Klein, *J. Biomed. Opt.* **2010**, *15*, 056018.
[19] T. A. Shaik, J. L. Lagarto, E. Baria, M. Goktas, P. Igoche Onoja, K. G. Blank, F. S. Pavone, J. Popp, C. Krafft, R. Cicchi, *Anal. Chem.* **2021**, *93*, 3813.
[20] T. A. Shaik, E. Baria, X. Wang, F. Korinth, J. L. Lagarto, C. Höppener, F. S. Pavone, V. Deckert, J. Popp, R. Cicchi, C. Krafft, *Anal. Chem.* **2022**, *94*, 1575.
[21] R. Cicchi, D. Kapsokalyvas, V. De Giorgi, V. Maio, A. Van Wiechen, D. Massi, T. Lotti, F. S. Pavone, *J. Biophotonics* **2010**, *3*, 34.
[22] J. Chen, S. Zhuo, X. Jiang, X. Zhu, L. Zheng, S. Xie, B. Lin, H. Zeng, *J. Biomed. Opt.* **2011**, *16*, 051305.
[23] A. Medyukhina, N. Vogler, I. Latka, S. Kemper, M. Böhm, B. Dietzek, J. Popp, *J. Biophotonics* **2011**, *4*, 627.
[24] M. Strupler, A.-M. Pena, M. Hernest, P.-L. Tharaux, J.-L. Martin, E. Beaurepaire, M.-C. Schanne-Klein, *Opt. Express* **2007**, *15*, 4054.
[25] T. Guilbert, C. Odin, Y. Le Grand, L. Gailhouste, B. Turlin, F. Ezan, Y. Désille, G. Baffet, D. Guyader, *Opt. Express* **2010**, *18*, 25794.
[26] L. Gailhouste, Y. Le Grand, C. Odin, D. Guyader, B. Turlin, F. Ezan, Y. Désille, T. Guilbert, A. Bessard, C. Frémin, N. Theret, *J. Hepathol.* **2010**, *52*, 398.
[27] S. V. Plotnikov, A. M. Kenny, S. J. Walsh, B. Zubrowski, C. Joseph, V. L. Scranton, G. A. Kuchel, D. Dauser, M. Xu, C. C. Pilbeam, D. J. Adams, R. P. Dougherty, P. J. Campagnola, W. A. Mohler, *J. Biomed. Opt.* **2008**, *13*, 044018.
[28] V. Tsafas, K. Giouroukou, K. Kounakis, M. Mari, C. Fotakis, N. Tavernarakis, G. Filippidis, *J. Biophotonics* **2021**, *14*, e202100173.
[29] O. Nadiarnykh, S. Plotnikov, W. A. Mohler, I. Kalajzic, D. Redford-Badwal, P. J. Campagnola, *J. Biomed. Opt.* **2007**, *12*, 051805.
[30] R. LaComb, O. Nadiarnykh, P. J. Campagnola, *Biophys. J.* **2008**, *94*, 4504.
[31] K. M. Reiser, C. Bratton, D. R. Yankelevich, A. Knoesen, I. Rocha-Mendoza, J. Lotz, *J. Biomed. Opt.* **2007**, *12*, 064019.
[32] N. Tiwari, S. Chabra, S. Mehdi, P. Sweet, T. B. Krasieva, R. Pool, B. Andrews, G. M. Peavy, *J. Biomed. Opt.* **2010**, *15*, 056001.
[33] S. J. Lin, C.-Y. Hsiao, Y. Sun, W. Lo, W.-C. Lin, G.-J. Jan, S.-H. Jee, C.-Y. Dong, *Opt. Lett.* **2005**, *30*, 622.
[34] P. Matteini, F. Ratto, F. Rossi, R. Cicchi, C. Stringari, D. Kapsokalyvas, F. S. Pavone, R. Pini, *Opt. Express* **2009**, *17*, 4868.
[35] T. Theodossiou, G. S. Rapti, V. Hovhannisyan, E. Georgiou, K. Politopoulos, D. Yova, *Lasers Med. Sci.* **2002**, *17*, 34.
[36] W. Lo, Y.-L. Chang, J.-S. Liu, C.-M. Hseuh, V. Hovhannisyan, S.-J. Chen, H.-Y. Tan, C.-Y. Dong, *J. Biomed. Opt.* **2009**, *14*, 054003.
[37] Y. Sun, W.-L. Chen, S.-J. Lin, S.-H. Jee, Y.-F. Chen, L.-C. Lin, P. T. C. So, C.-Y. Dong, *Biophys. J.* **2006**, *91*, 2620.
[38] C. Bodelon, M. Mullooly, R. M. Pfeiffer, S. Fan, M. Abubakar, P. Lenz, P. M. Vacek, D. L. Weaver, S. D. Herschorn, J. M. Johnson, B. L. Sprague, S. Hewitt, J. Shepherd, S. Malkov, P. J. Keely, K. W. Eliceiri, M. E. Sherman, M. W. Conklin, G. L. Gierach, *Breast Cancer Res.* **2021**, *23*, 105.
[39] R. Mercatelli, T. Triulzi, F. S. Pavone, R. Orlandi, R. Cicchi, *J. Biophotonics* **2020**, *13*, e202000159.
[40] V. Tsafas, I. Oikonomidis, E. Gavgiotaki, E. Tzamali, G. Tzedakis, C. Fotakis, I. Athanassakis, G. Filippidis, *IEEE J. Biomed. Health Inform.* **2022**, *26*, 1188.
[41] V. Tsafas, E. Gavgiotaki, M. Tzardi, E. Tsafa, C. Fotakis, I. Athanassakis, G. Filippidis, *J. Biophotonics* **2020**, *13*, e202000180.
[42] Z. H. Zhou, C. D. Ji, H. L. Xiao, H. B. Zhao, Y. H. Cui, X. W. Bian, *J. Cancer* **2017**, *8*, 1466.
[43] G. Wang, Y. Sun, S. Jiang, G. Wu, W. Liao, Y. Chen, Z. Lin, Z. Liu, S. Zhuo, *Biomed. Opt. Express* **2021**, *12*, 5658.
[44] S. Z. Despotovic, Đ. N. Milićević, A. J. Krmpot, A. M. Pavlović, V. D. Živanović, Z. Krivokapić, V. B. Pavlović, S. Lević, G. Nikolić, M. D. Rabasović, *Sci. Rep.* **2020**, *10*, 6359.
[45] N. Kiss, D. Haluszka, K. Lőrincz, N. Gyöngyösi, S. Bozsányi, A. Bánvölgyi, R. Szipőcs, N. Wikonkál, *Pathol. Oncol. Res.* **2019**, *25*, 1015.
[46] D. Tokarz, D. R. Cisek, A. Joseph, A. Golaraei, K. Mirsanaye, S. Krouglov, S. L. Asa, B. C. Wilson, V. Barzda, *Front. Oncol.* **2019**, *9*, 272.
[47] S. Psilodimitrakopoulos, S. I. Santos, I. Amat-Roldan, A. K. Thayil, D. Artigas, P. Loza-Alvarez, *J. Biomed. Opt.* **2009**, *14*, 014001.
[48] K. P. Quinn, I. Georgakoudi, *J. Biomed. Opt.* **2013**, *18*, 046003.
[49] E. A. Sander, V. H. Barocas, *J. Biomed. Mater. Res., Part A* **2009**, *88*, 322.
[50] Z. Puspoki, M. Storath, D. Sage, M. Unser, *Adv. Anat. Embryol. Cell. Biol.* **2016**, *219*, 69.
[51] Y. Liu, A. Keikhosravi, C. A. Pehlke, J. S. Bredfeldt, M. Dutson, H. Liu, G. S. Mehta, R. Claus, A. J. Patel, M. W. Conklin, D. R. Inman, P. P. Provenzano, E. Sifakis, J. M. Patel, K. W. Eliceiri, *Front. Bioeng. Biotechnol.* **2020**, *8*, 198.
[52] Y. Liu, A. Keikhosravi, G. S. Mehta, C. R. Drifka, K. W. Eliceiri, *Methods Mol. Biol.* **2017**, *1627*, 429.

[53] A. Rassoli, N. Fatouraee, R. Guidoin, Z. Zhang, *Artif. Organs* **2020**, *44*, 278.
[54] W. R. Zipfel, R. M. Williams, W. W. Webb, *Nat. Biotechnol.* **2003**, *21*, 1369.
[55] M. Marchetti, E. Baria, R. Cicchi, F. S. Pavone, *Methods Protoc.* **2019**, *2*, 51.
[56] M. Hall-Beyer, GLCM Texture: A Tutorial v. 3.0. **2017** https://prism.ucalgary.ca/items/8833a1fc-5efb-4b9b-93a6-ac4ff268091c (accessed: February 2024)
[57] S. Singh, D. Srivastava, S. Agarwal, in *2017 5th Int. Symp. Comput. Bus. Intell.*, 20, IEEE. **2017**.
[58] E. Baria, G. Nesi, R. Santi, V. Maio, D. Massi, C. Pratesi, R. Cicchi, F. S. Pavone, *J. Biophotonics* **2018**, *11*, e201800106.
[59] J. S. Bredfeldt, Y. Liu, C. A. Pehlke, M. W. Conklin, J. M. Szulczewski, D. R. Inman, P. J. Keely, R. D. Nowak, T. R. Mackie, K. W. Eliceiri, *J. Biomed. Opt.* **2014**, *19*, 016007.
[60] A. Picon, A. Medela, L. F. Sanchez-Peralta, R. Cicchi, R. Bilbao, D. Alfieri, A. Elola, B. Glover, C. L. Saratxaga, *IEEE Access* **2021**, *9*, 32081.
[61] J. M. Burel, S. Besson, C. Blackburn, M. Carroll, R. K. Ferguson, H. Flynn, K. Gillen, R. Leigh, S. Li, D. Lindner, M. Linkert, W. J. Moore, B. Ramalingam, E. Rozbicki, A. Tarkowska, P. Walczysko, C. Allan, J. Moore, J. R. Swedlow, *Mamm. Genome* **2015**, *26*, 441.

How to cite this article: R. Cicchi, E. Baria, M. Mari, G. Filippidis, D. Chorvat, *J. Biophotonics* **2024**, e202400090. https://doi.org/10.1002/jbio.202400090